Monthly Notices
of the
ROYAL ASTRONOMICAL SOCIETY

MNRAS **484,** 5362–5376 (2019)
Advance Access publication 2019 January 28

doi:10.1093/mnras/stz298

Evidence for bimodal orbital separations of white dwarf–red dwarf binary stars

R. P. Ashley,[1]★ J. Farihi,[2] T. R. Marsh,[1] D. J. Wilson[1] and B. T. Gänsicke[1]

[1]*Department of Physics, University of Warwick, Gibbet Hill Road, Coventry, West Midlands CV4 7AL, UK*
[2]*Department of Physics and Astronomy, University College London, Gower St, Kings Cross, London WC1E 6BT, UK*

Accepted 2019 January 25. Received 2019 January 24; in original form 2018 November 22

ABSTRACT

We present the results of a radial velocity survey of 20 white dwarf plus M dwarf binaries selected as a follow up to a *Hubble Space Telescope* study that aimed to spatially resolve suspected binaries. Our candidates are taken from the list of targets that were spatially unresolved with *Hubble*. We have determined the orbital periods for 16 of these compact binary candidates. The period distribution ranges from 0.141 to 9.16 d and peaks near 0.6 d. The original sample therefore contains two sets of binaries, wide orbits (≈100–1000 au) and close orbits ($\lesssim$1–10 au), with no systems found in the ≈10–100 au range. This observational evidence confirms the bimodal distribution predicted by population models and is also similar to results obtained in previous studies. We find no binary periods in the months to years range, supporting the post-common envelope evolution scenario. One of our targets, WD 1504+546, was discovered to be an eclipsing binary with a period of 0.931 d.

Key words: binaries: general – stars: evolution – stars: formation – stars: low-mass – stars: luminosity function, mass function – white dwarfs.

1 INTRODUCTION

It is estimated that the field star population in the solar neighbourhood consists of 50 per cent binary systems (Eggleton & Tokovinin 2008). During the evolutionary lifetime of these systems many can evolve into compact binaries. Compact binaries are some of the most interesting objects in the Galaxy, and include the precursors to type Ia supernovae that are the cosmic yardsticks used to measure inter-galactic distances and, consequently, the scale of the universe. Compact binary evolution is also the path that leads to the formation of a pair of neutron stars that, when merging, produce the gravitational wave signals that are now being detected by LIGO and VIRGO. Other examples are X-ray binaries, double-degenerate binaries (Nelemans & Tout 2005), planetary nebulae (De Marco 2009), and cataclysmic variables (Tappert et al. 2009).

A fundamental phase in the evolution of these systems is the *common envelope*. After their initial formation, both components in a binary system live out their main-sequence lives without interaction, but when the more massive component, the primary star, leaves the main sequence, it will evolve up the red giant branch. If the separation of the components in the binary is sufficiently small, the primary star's increase in size will be such that it fills the Roche lobe. At this point unstable mass transfer is triggered and the primary's atmosphere will extend sufficiently far to engulf both stars and thereby form a common envelope. During the common envelope phase, drag forces will drain angular momentum from both bodies and bring them closer. This angular momentum is transferred to the gas envelope and helps to expel it from the system. The exact processes that occur during the common envelope phase are poorly understood, and difficult to model computationally, but it is thought that the inspiral occurs quickly (<100 yr; Ivanova et al. 2013). Eventually, the primary will evolve away from its giant phase, leaving behind a white dwarf. The end result of this process is a pair consisting of a white dwarf and a main-sequence star (WD+MS) with a relatively small separation, known as a post-common envelope binary (PCEB). However, not all binary systems will follow this path. If the initial separation of the two components is larger than about 2–3 au (Willems & Kolb 2004), then the red giant star does not fill its Roche lobe and no common envelope is formed. In fact, when the outer atmosphere of the primary is dissipated, this mass-loss will have the effect of widening the orbit. These two distinct evolutionary paths lead to two separate populations of WD+MS binaries, those that have experienced a common envelope and therefore have periods of hours to days, and those that have not experienced a common envelope and have periods of several years or more.

A commonly used method to investigate the outcome of the common envelope phase is Binary Population Synthesis (BPS). This is a theoretical process that involves simulating the evolution of a binary by modelling the development of both components using stellar evolution models and including additional simulations of mass transfer and orbital dynamics (Willems & Kolb 2004). BPS studies have been performed for Type Ia supernova progenitors

★ E-mail: r.p.ashley@warwick.ac.uk

(Han & Podsiadlowski 2004), short γ-ray bursts (Belczynski et al. 2006), and, most useful for this study, WD+MS systems (Willems & Kolb 2004; Davis, Kolb & Willems 2010). These studies predict that WD+MS systems will have orbital periods that follow a bimodal distribution, with the short-period PCEBs peaking at about 1–2 d [$\log P_{\rm orb}$ (d) ≈ 0.2], and continuously detached binaries with periods of years or more.

The fraction of the orbital energy that goes into discarding the common envelope is usually given as $\alpha_{\rm CE}$ where $E_{\rm bind} = \alpha_{\rm CE}\Delta E_{\rm orb}$. $E_{\rm bind}$ is the gravitational binding energy of the envelope and $\Delta E_{\rm orb}$ is the change in orbital energy of the two stars (Willems & Kolb 2004; Davis et al. 2010; Zorotovic et al. 2014). Recent observational and theoretical studies indicate a value for the efficiency of transfer of the orbital energy $\alpha_{\rm CE} = 0.2$–0.3 (Zorotovic et al. 2010).

An additional energy source that might be a factor in dispersing the common envelope is the recombination energy released when the ionized hydrogen gas in the common envelope is neutralized. Zorotovic et al. (2014) show that increasing the contribution that recombination energy plays in the dispersal of the envelope would lead to longer period PCEBs overall with a tail in the period distribution going out to about 1000 d, since this energy would contribute to the dispersal of the common envelope and less energy would be needed from the angular momentum loss. At the moment no PCEB systems are known to have periods of this length. The longest known PCEB period is that of IK Peg at 21.72 d (Landsman 1993).

In order to test the underlying period distribution of WD+MS binaries, we need an observationally derived period distribution of an unbiased sample. In recent years, large-scale surveys such as Sloan Digital Sky Survey (SDSS; Alam et al. 2015) have enabled the study of the orbital period distribution of a sample of WD+MS binaries and measurement of the fraction of those that have undergone a common envelope phase (Schreiber et al. 2008, 2010; Nebot Gómez-Morán et al. 2011; Rebassa-Mansergas et al. 2012). These studies have shown broad agreement with predictions of the fraction of PCEBs versus widely separated binaries and the shape of the period distribution for the PCEBs themselves. Nebot Gómez-Morán et al. (2011) concluded that about a third of the WD+MS binaries identified by SDSS are short-period PCEBs, and the rest are candidate wide binaries. These are systems that, at the SDSS imaging resolution, ≈1–2 arcsec, are still unresolved, but since they are at distances of a few 100 pc, they could have separations of 100 au or more.

In this study, we used spectroscopy to search for radial velocity variations in 20 WD+MS binaries to ascertain if they are PCEB systems. We started with a sample created by Farihi, Hoard & Wachter (2006) that was selected by searching for white dwarfs with near-infrared excess. Our targets were chosen from those that were shown to be unresolved in images taken by the *Hubble Space Telescope* (*HST*). In the context of post-common envelope evolution, theory predicts these systems should all be close binaries.

2 OBSERVATIONS

2.1 Target selection

Farihi, Hoard & Wachter (2010) obtained *HST* high-resolution imaging of WD+MS binaries to test the bimodal period distribution with an unbiased sample. The targets selected were chosen from the McCook & Sion (1999) catalogue of white dwarfs, which were found to exhibit a near-infrared excess in 2MASS photometry by Wachter et al. (2003). A complete list of the original targets can be found in table 1 of Farihi et al. (2006).

The Advanced Camera for Surveys (ACS) High-Resolution Camera (HRC) was used to image these targets with the F814W filter to try to resolve each suspected binary. The results of this exercise can be seen in table 7 of Farihi et al. (2010), where it was found that 72 of the 90 candidates were highly probable binaries and, of these, 43 systems were spatially resolved with the ACS HRC. Combining the angular separation with distance estimates to each target allowed Farihi et al. (2010) to compute the minimum value for the semimajor axis (at zero inclination) for each binary pair.

The remaining 29 systems were unresolved at the resolution of the *HST* imaging. Taking the spatially resolved limit of one pixel on the ACS HRC camera (0.025 arcsec) as the resolving power of the imaging study, it was possible to place upper limits on the apparent separation on these unresolved targets. At the distances to these targets, the limits are about 10 au, corresponding to orbital periods of tens of years. In this study, we have attempted to obtain radial velocity measurements of these systems.

We obtained spectroscopy of 20 of the 29 WD+MS binaries that were accessible from the Isaac Newton Telescope at the Roque de los Muchachos Observatory, Canary Islands, Spain. To constrain and potentially determine the orbital periods, the observations were taken in the *I*-band (6500–9000 Å) region to measure features in the atmosphere of the secondary, and monitor them for radial velocity variations. The Na I doublet at 8183.3 and 8194.8 Å and the Hα line at 6562.8 Å were used.

As a follow up to our spectroscopy, we examined the archives of the Catalina Real-time Transient Survey (CRTS; Drake et al. 2014) and the Palomar Transient Factory (PTF; Law et al. 2009) to look for photometric observations for all of our targets. We discovered that of our 20 systems, 16 had CRTS photometry and 10 had PTF photometry. In the cases of WD 0303−007, WD 1458+171, and WD 1504+546, these data provided additional insight and this is discussed in Section 4.

2.2 Reduction

The spectra were obtained using the Intermediate Dispersion Spectrograph (IDS) with the R831R grating. This is a medium dispersion grating with a dispersion of 0.75 Å per pixel and a resolving power of $R = 4667$ at 7000 Å. The central wavelengths were chosen to ensure that features of interest were placed near the centre of the detector, 8200 Å for the Na I doublet and 6560 Å for Hα. A summary of our observations is shown in Table 1.

Each observing night included at least two standard stars in order to enable flux calibration and the removal of telluric features. All of the spectra were optimally extracted and reduced using the PAMELA and MOLLY reduction software (Marsh 1989). Our comparison stars were chosen from early-type main-sequence stars and white dwarfs since their spectra have few features in the 7500–8700 Å region. A list of these standards is given in Table A2. We fitted splines to the continua of our comparison stars, avoiding regions of atmospheric absorption from 7560 to 7690 Å and 8100 to 8400 Å. The ratio of the fit to the original spectrum was then used to correct for the absorption in the target spectra (see e.g. Marsh 1990). The calibration star with the nearest airmass was used and the correction was scaled by the ratio of the airmasses to the power 0.55 to account for the saturated absorption bands. The removal of these significant telluric features was not always adequate and this meant that some

Table 1. The targets observed during the campaign. The coordinates are in epoch J2000. Spectra were deemed unusable if we were unable to fit a profile to the Na I or H α feature. For all targets the Na I doublet at 8190 Å was observed, with the exception of WD+162, where we observed the H α emission from the secondary.

WD	RA (h m s)	Dec (° ′ ″)	# Spectra taken	# Usable spectra
0023+388	00 26 33.2	+39 09 03	21	15
0303−007	03 06 07.1	−00 31 14	31	31
0354+463	03 58 17.1	+46 28 41	57	46
0430+136	04 33 10.3	+13 45 17	30	29
0752−146	07 55 08.9	−14 45 53	30	20
0812+478	08 15 48.9	+47 40 39	16	16
0908+226	09 11 43.1	+22 27 49	26	23
1001+203	10 04 04.2	+20 09 23	22	22
1037+512	10 40 16.8	+50 56 47	22	22
1051+516	10 54 21.9	+51 22 54	22	22
1133+358	11 35 42.7	+35 34 24	19	19
1333+487	13 36 01.7	+48 28 45	17	8
1339+606	13 41 00.0	+60 26 10	20	12
1433+538	14 34 43.1	+53 35 25	26	22
1436−216	14 39 12.8	−21 50 12	32	32
1458+171	15 00 19.4	+16 59 16	18	10
1504+546	15 06 05.3	+54 28 19	39	39
1517+502	15 19 05.9	+50 07 03	22	0
2257+162	22 59 46.9	+16 29 17	16	14
2317+268	23 20 04.1	+25 52 21	12	11

spectra could not be used for radial velocity fits as the Na I features were not visible after this correction.

For wavelength calibration, CuNe and CuAr arcs were observed several times over the course of the observations. This was then further improved by examining sky emission features in each of the science and calibration spectra and calculating the final wavelength shift required to assign these features to their known wavelengths. The sky emission lines used were the oxygen emission features at 7913.7 and 8344.6 Å.

3 ANALYSIS

Radial velocities for all spectra were calculated by least-squares fit of a double-Gaussian function to the data near the Na I doublet at 8190 Å. The separation of the doublet was kept fixed at the laboratory value of 11.5 Å; the depth of the lines was free to vary but kept equal to each other, and the width of the lines was fixed to an FWHM of 2.4 Å. One of the targets, WD 1001+203, showed consistently broad lines on all of the spectra, so for this object, a larger width of 4.7 Å was used. The uncertainties of the fit parameters were taken from the co-variance matrix produced in the Levenberg–Marquardt procedure. The fitted wavelengths were then converted to radial velocities by calculating the shift to the rest wavelength for the blue-ward line of the doublet, 8183.3 Å.

For the target WD 2257+162, it was noted that previous observations had been unable to detect the Na I doublet (Liebert, Bergeron & Holberg 2005; Tremblay & Bergeron 2007), and therefore spectra centred on the H α line were taken. Two overlapping Gaussian functions, one representing the emission profile and a second for the absorption profile, were fitted. Radial velocities were derived by comparing the wavelength to the rest wavelength of H α. While the fit to the emission gave errors of about 10 km s^{-1}, similar to measurements of the Na I doublet for the other targets, the absorption feature was too broad to allow the determination of the radial velocity of the white dwarf. The measured radial velocities for all of the targets are listed in Table A1 of the Appendix.

Table 2. Fitted periods and aliases shown with the corresponding reduced χ^2 value. For each target, the number of valid radial velocity measurements N used in the analysis is also shown. We show the next best competing alias along with the associated increase in χ^2.

WD	N	$P_{\rm orb}$ (d)	$\chi^2_{\rm red}$	2nd best alias (d)	$\Delta\chi^2$
0023+388	19	0.641 59(1)	1.2	0.683 39(1)	12
0303−007	31	0.541 13(1)	1.0	1.190 96(4)	135
0354+463	46	0.165 203(1)	1.0	0.246 896(2)	154
0430+136*	30	0.135 480(7)	0.2	0.119 120(6)	0
0752−146	21	1.052 41(3)	1.0	0.522 410(5)	15
0812+478*	16	0.055 373(1)	0.2	0.7141(2)	0
0908+226	22	9.1614(8)	0.5	9.393(8)	2
1001+203*	22	0.265 79(2)	0.2	0.209 13(2)	0
1037+512	26	0.141 460(1)	0.5	0.165 146(2)	1
1051+516	22	2.770 208(3)	0.5	0.733 22(2)	16
1133+358	18	5.956(2)	0.0	6.055(2)	0
1333+487	11	1.755 84(2)	0.0	2.275 44(7)	1
1339+606	17	0.493 67(1)	0.4	0.247 534(4)	0
1433+538	22	4.479(3)	0.4	4.357(2)	0
1436−216	32	2.017 74(2)	0.4	0.669 88(4)	5
1458+171	10	0.079 3902(3)	1.5	0.164 702(1)	5
1504+546	36	0.930 72(2)	1.0	0.479 524(5)	128
2257+162	15	0.3223(1)	0.7	0.4736(5)	21
2317+268	10	0.7944(9)	1.0	3.85(5)	0

Notes. (∗) No significant radial velocity variation detected.

3.1 Binary periods

In order to identify which of the targets exhibited radial velocity variability, we used a test described in Maxted et al. (2008), where we calculate the probability, p, of obtaining the computed χ^2 value compared to that computed from a sample of measurements distributed normally around the mean radial velocity. We set the criterion for radial velocity detection to $\log(p) < -4$. The three targets that did not meet this criterion were WD 0430+221, WD 0812+478, and WD 1001+203. We were unable to detect any Na I absorption lines in our spectra of WD 1517+302 and therefore could not deduce any radial velocity variability for this system.

Periods were derived by fitting a sine wave plus a constant to the data, and choosing the frequency that corresponded to the lowest χ^2. Our algorithm used the floating mean periodogram approach (Cumming, Marcy & Butler 1999). The key point in this method is that the constant systemic velocity is fitted at the same time as semi-amplitude and phase. This corrects a failing of the well-known Lomb–Scargle (Lomb 1976; Scargle 1982) periodogram that starts by subtracting the mean of the data and then fits a plain sinusoid and this is incorrect for small numbers of points.

The data sampling that occurred as a result of our observing strategy, i.e. taking a spectrum once or twice per night during a week-long run, means that we were susceptible to aliasing, especially at multiples of 1 d^{-1}. We also had long gaps of several months between observing runs, which caused a fine splitting of the 1 d aliases. Although it is certain that the radial velocities measured are due orbital motion and also that the periods are relatively short (of the order of days), in some cases there are several competing aliases. Table 2 lists the best period and the most significant competing alias. Fig. B1 shows the fitted radial velocity plots and periodograms for all 19 of the objects that had

Table 3. Parameters for the binaries determined from the radial velocity study. The period, K_2, and γ_2 velocities are from this paper, the secondary estimated spectral type is taken from Farihi et al. (2010), and the $T_{\rm eff}$ has been retrieved from the Montreal White Dwarf Database (Dufour et al. 2017).

WD	$P_{\rm orb}$ (d)	K_2 (km s^{-1})	γ_2 (km s^{-1})	SpType	$T_{\rm eff}$ (K)
0023+388	0.641 59(1)	153(4)	−24(3)	DA+dM5.5	10 980
0303−007	0.541 13(1)	132(3)	6(2)	DA+dM4	20 310
0354+463	0.165 203(1)	115(3)	−67(2)	DA+dM7	8230
0430+136	–	–	–	DA+dM5.5	34 210
0752−146	1.052 41(3)	159(10)	0(13)	DA+dM6	19 440
0812+478	–	–	–	DA+dM4	62 000
0908+226	9.1614(8)	48(4)	−35(4)	DA+dM3	10 548
1001+203	–	–	–	DA+dM2.5	21 010
1037+512	0.141 460(1)	18(4)	−46(3)	DA+dM4	19 780
1051+516	2.770 208(3)	81(3)	10(2)	DA+dM3	23 863
1133+358	5.956(2)	78(3)	−17(3)	DC+dM4.5	6500
1333+487	1.755 84(2)	153(9)	−81(9)	DB+dM6.5	14 676
1339+606	0.493 67(1)	73(9)	−2(6)	DA+dM3.5	44 770
1433+538	4.479(3)	81(4)	−44(3)	DA+dM4.5	23 260
1436−216	2.017 74(2)	44(10)	−4(2)	DA+dM2.5	23 690
1458+171	0.164 702(1)	180(8)	23(6)	DA+dM4.5	22 600
1504+546	0.930 72(2)	129(4)	−3(3)	DA+dM3	23 120
1517+502	–	–	–	DA+dC	31 270
2257+162	0.3223(1)	74(7)	16(5)	DA+dM4.5	25 450
2317+268	0.7941(2)	125(6)	12(4)	DA+dM3.5	31 890

fitted radial velocity data. This figure includes the three targets, WD 0430+136, WD 0812+478, and WD 1001+203 that failed the radial velocity variability test but are shown here for completeness.

Once the best frequency had been identified, it was used as a starting point for a least-squares fit of a sine wave to the data of the following form:

$$v_{\rm r} = \gamma_2 + K_2 \sin\left[\frac{2\pi(t - t_0)}{P_{\rm orb}}\right], \quad (1)$$

where the initial guess for $P_{\rm orb}$ was $1/f$ and f is the frequency at the lowest χ^2 on the periodogram and allowed to vary in the fit, γ_2 is the systemic velocity of the secondary star, t_0 is the zero-point defined by the inferior conjunction of the secondary star, and K_2 is the radial velocity semi-amplitude of the secondary star.

Fig. B1 shows the reduced χ^2 value for each of the fitted radial velocity curves. Several systems showed clear signs of extra noise, with minimum χ^2 values much larger than the number of degrees of freedom. Particularly discrepant spectra were examined for signs of problems, and the conclusion drawn was that the most likely cause was residual and/or poorly corrected telluric absorption. Non-uniform filling of the spectrograph slit could have also been a contributing factor. In order to account for this extra source of noise, a fixed value was added, in quadrature, to all uncertainties to make the reduced χ^2 equal to unity for each fit. The typical fixed value added to the uncertainties was 7–10 km s^{-1}. This corresponds to about one third of a pixel in the spectrograph dispersion. Experience shows that this is a little larger than typical fluctuations caused by non-uniform slit illumination, hence we suspect that telluric correction is the more significant issue. Although this noise reduces the precision of our data, the radial velocity signal in most of our targets leaves no doubt as to the reality of the variations.

For all targets, the χ^2 value for the second best alias was also calculated. These values are listed in Table 2. It can be shown that the probability of a given period being the correct one in a Bayesian sense scales as $e^{-\chi^2/2}$ (Marsh, Dhillon & Duck 1995; Morales-Rueda et al. 2003). This means that for large values of $\Delta\chi^2$ we can be sure of our period, but for values of $\Delta\chi^2 < 5$ there is a significant chance of the correct period being one of the other aliases. Examination of Table 2 indicates that, while we can be sure that WD 0908+226, WD 1037+512, WD 1133+358, WD 1333+487, WD 1339+606, WD 1433+53, and WD 2317+268 exhibit radial velocity variability, we have not determined the true period with a high level of confidence.

Table 4. Resulting separation statistics for the subsamples of the 90 WD+MS binary candidates from Farihi et al. (2006), classified by separation.

Type	Number	Fraction
Candidates	90	–
Confirmed as binary	72	100 per cent
Resolved with *HST* (3–1000 au)	43	60 per cent
Unresolved ($\lesssim$ 10 au)	29	40 per cent
Included in this study	20	100 per cent
Confirmed as short period ($\lesssim$10 au)	17	85 per cent
Number with confirmed periods	16	–
Short period suspected, but no solution	1	–
Undetected radial velocity variability	3	15 per cent

Table 3 lists the derived periods for all of the objects. These range from 3.4 h to 9.2 d with the centre (the median in log $P_{\rm orb}$ terms) at $\approx$1 d. Since there are only 16 periods in our sample, it was difficult to fit a Gaussian to the period distribution although it has been estimated at around log $P_{\rm orb}$ (d) = −0.2 or P = 0.6 d, see Fig. 1.

In a similar study of systems selected from the SDSS undertaken by Nebot Gómez-Morán et al. (2011), it was found that the periods range from 1.97 h to 4.35 d, and approximately follow a normal distribution in log $P_{\rm orb}$ with a peak centred on $P_{\rm orb}$ = 8.1 h or $P_{\rm orb}$ = 0.34 d, Figs 1 and 2 show a comparison between that sample and this one. Their study had 79 targets, while this only contains 16 with determined periods. We performed an Anderson–Darling test (Scholz & Stephens 1987) on the two samples to check if they can

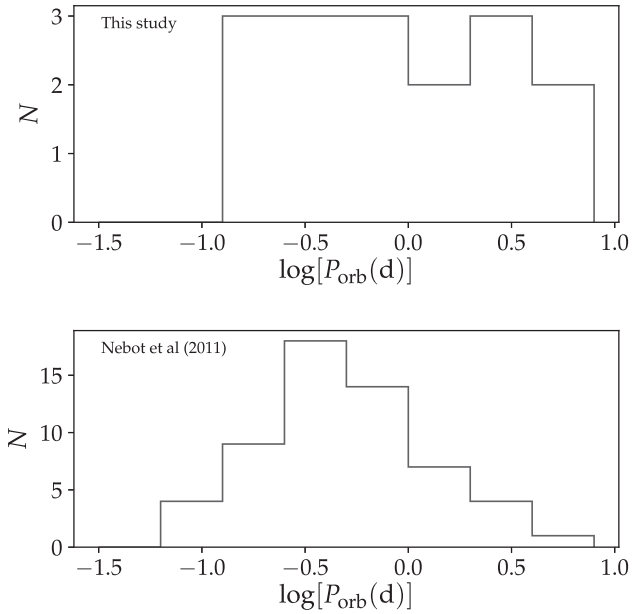

Figure 1. The orbital period distribution of the 16 PCEBs contained in this study compared to that of the 79 PCEBs characterized by Nebot Gómez-Morán et al. (2011).

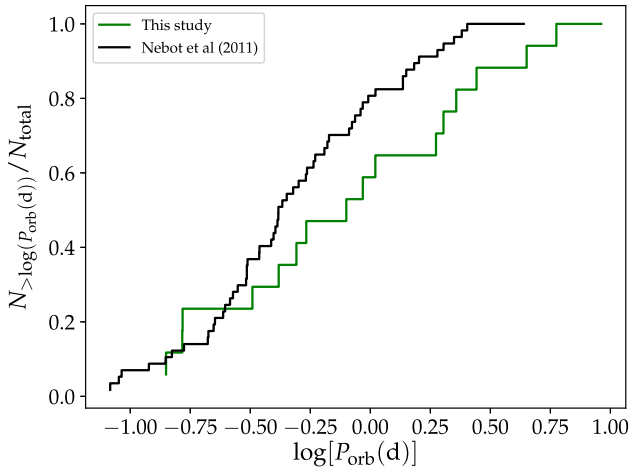

Figure 2. Comparison of the cumulative period distribution of this study and the period distribution of 79 PCEBs selected from SDSS by Nebot Gómez-Morán et al. (2011).

be considered as being derived from the same underlying population distribution. The results of this test suggest that we cannot reject the null hypothesis, i.e. that the two populations are not selected from the same underlying distribution at a 10 per cent level.

We also performed an Anderson–Darling test on our sample against the predicted population distribution in Willems & Kolb (2004). The cumulative distribution function is shown in Fig. 3. In this case the result suggests we can reject the null hypothesis at a 1 per cent level. From this we can conclude that our population does not match the distribution proposed in their BPS and has a peak in period distribution at a shorter duration as can be seen in Fig. 3. It should be noted that the Willems–Kolb study adopted a value of $\alpha_{CE} = 1$. In a more recent study, Davis et al. (2010) produced population distributions for two additional values of $\alpha_{CE} = 0.1$ and 0.6. They find that for low-mass secondaries (as per our sample) the

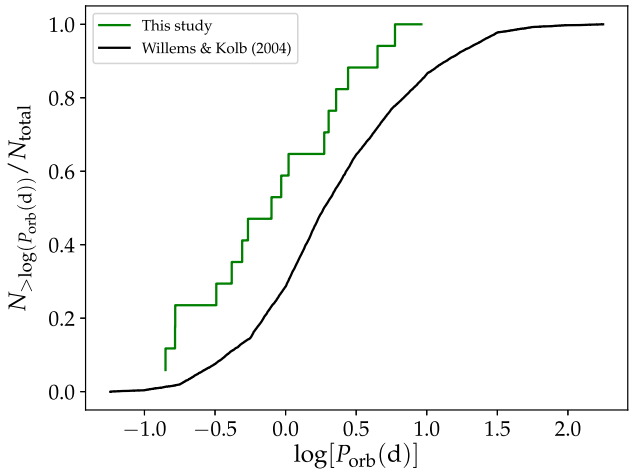

Figure 3. Comparison of the cumulative period distribution with a synthetic sample generated from the probability distribution for PCEB periods described in Willems & Kolb (2004). The Anderson–Darling test suggests the null hypothesis cannot be rejected at a 99 per cent confidence level.

theoretical period distribution peaks at log P_{orb} (d) ≈ -0.5, which is near to our peak at log P_{orb} (d) ≈ -0.2. Davis et al. (2010) conclude that a value of $\alpha_{CE} = 0.1$ will predict the observed peak in period distribution, but the distribution will also include a long tail at longer periods going out to hundreds of days. Binaries with such a long period have not yet been observed among PCEB systems and this includes those in the present study.

More recently, Camacho et al. (2014) show that for the PCEBs selected from SDSS, small values for the common envelope efficiency ($\alpha_{CE} < 0.3$) in simulated populations predict the observed period distribution. Our study, though limited in sample size, agrees with these modelled values of α_{CE}.

In the *HST* imaging survey of Farihi et al. (2010), 72 of the 90 targets were confirmed to be WD+MS binaries with the remaining stars deemed to be non-binary. Of the binaries, 43 were resolved with ACS HRC imaging, implying separations wider than at least a few au. The remaining 29 were unresolved with *HST*. We obtained spectroscopy for 20 of the unresolved pairs, of which 16 were confirmed as short-period (∼hours to days) systems that underwent a common envelope phase. Thus overall, about 60 per cent of the binaries have wide orbits and 34 per cent are in close orbits with the remaining 6 per cent not determined.

Nebot Gómez-Morán et al. (2011) calculated a 23 ± 2 per cent PCEB fraction for WD+MS systems found in SDSS, with an upper limit, after taking selection effects into account, of 27 per cent. In our smaller sample, we obtain a PCEB fraction of 34 per cent, but our sample is biased as it excluded targets that were spatially resolved in ground-based images. Accounting for the fact that spatially resolved binaries are 63 per cent of the population when viewed from the ground (Farihi et al. 2006), the PCEB fraction of this study reduces to 22 per cent, and is similar to the 23 per cent of Nebot Gómez-Morán et al. (2011).

While the difference between the results from this study and that of Nebot Gómez-Morán et al. (2011) is not statistically significant, it is noted that there is a tendency for slightly longer periods here. Zorotovic et al. (2011) find evidence of a trend towards longer periods for PCEBs with an earlier secondary. Comparison of the secondary spectral types between the Nebot study and this one indicates that there is no discernible difference with both distributions having a median value of approximately M4. Therefore, although this study

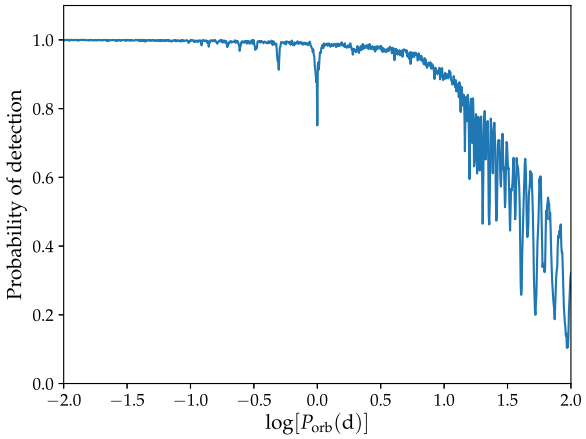

Figure 4. The detection probability of radial velocity variations for a simulated input population with periods following a flat distribution in $-2 \leq \log P_{orb} \geq 2$. The detection is modelled on our actual observation times and instrument set-up, as described in the text.

hints at confirmation of this relationship between secondary spectral type and period, we cannot confirm it conclusively.

3.2 Observational constraints

In order to understand the effects of our experimental approach in terms of instrument sensitivity and measurement cadence, we performed a Monte Carlo simulation on a synthetic sample of input period distributions. For each period in our input sample, we assumed a random orientation for the inclination of the system with a distribution that is flat in $\cos(i)$. We then calculated a K_2 amplitude using the mass function,

$$\frac{(M_1 \sin(i))^3}{(M_1 + M_2)^2} = \frac{P_{orb} K_2^3}{2\pi G}, \quad (2)$$

where G is the gravitational constant. For the masses of the binaries, we assumed values of $M_1 = 0.6\,M_\odot$ and $M_2 = 0.2\,M_\odot$ for all of the objects in the simulation. We randomly selected an HJD based on the actual observing dates and times and computed the simulated observed K_2 velocity. We used 15 km s^{-1} as the limit on the standard deviation of the simulated velocities to distinguish a detection of radial velocity variation. We repeated this test for 1000 input periods to deduce the detection probability as a function of orbital period. The input periods were selected from a random distribution of uniform probability for periods in the range $-2.0 \leq \log P_{orb}(d) \leq 2.0$. The results are shown in Fig. 4. We can be confident that our observing strategy will detect systems with periods ranging from 0.01 to ≈10 d but the detection rate drops off markedly for periods greater than 30 d. In additional simulations, we tweaked two factors: (a) the observation baseline, by creating an artificially extended set of observation times and (b) an improved observation error, by artificially reducing our measurement error on the wavelength of the spectral features. The former simulation did not lead to improvement in the detectability of longer period systems, but the latter significantly improved the chances of finding radial velocities for systems with periods longer than 10 d. From this we can conclude that our observational set-up is limited by the grating resolution and the signal-to-noise (S/N) of our targets at the telescope and not the time baseline of our observations.

The three objects that showed no detectable radial velocity variations could have periods that fall into the weeks to several years range and have escaped our detection regime at the INT. Our simulations suggest that improving our radial velocity sensitivity through higher S/N spectra and higher resolution gratings may allow us to detect periods in such systems.

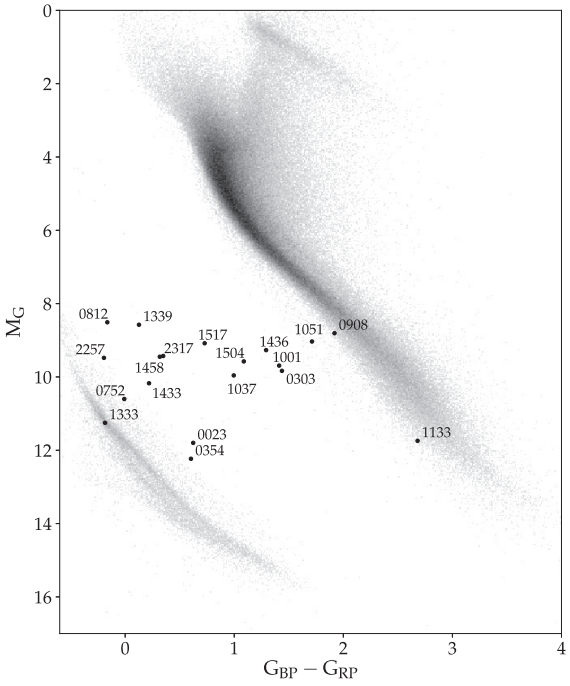

Figure 5. Colour–magnitude diagram showing the position of our objects relative to the white dwarf and main sequence. The only member of our sample that is not present in this diagram is WD 0430+136, which does not have a published parallax in *Gaia* DR2.

3.3 Position on the HR diagram

With one exception (WD 0430+136), all of our targets have *Gaia* measured parallaxes in DR2 (Gaia Collaboration 2018). Using these data, we are able to place the binaries on the HR diagram. All points lie between the white dwarf and main sequence as shown in Fig. 5. Some of the objects are at the extreme edges of this range and we discuss those in the following section.

In Fig. 5, the data used for indicating the overall population of the solar neighbourhood were drawn from a random sample of 327 000 entries in DR2 that matched the quality criterion that the G magnitude was greater than 20 times the error in the G magnitude. To increase the visibility of the white dwarf sequence, we supplemented the sample with a selected set of 14 000 white dwarfs drawn from DR2 by colour selection.

4 NOTES ON INDIVIDUAL OBJECTS

0303-007. Phase folding the CRTS data to our radial velocity derived period reveals a tentative increase in brightness by about 0.05 mag at phase 0.5 as shown in Fig. 6. This could be due to a small reflection effect on the secondary.

0354+463. Zuckerman et al. (2003) identify this target as containing a DAZ and report that the velocity of the Ca II K absorption in the white dwarf and the Hβ emission line in the M dwarf agree reasonably well at −69.7 and −67.7 km s^{-1}, respectively. We measured a γ_2 velocity of −67 km s^{-1} using the Na I absorption in the secondary. The metal pollution of the white dwarf atmosphere

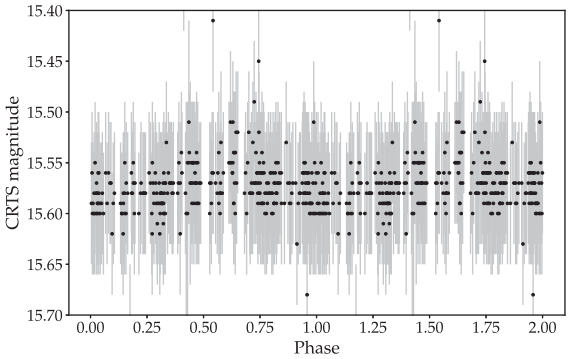

Figure 6. The phased-folded CRTS light curve of WD 0303-007. At phase 0.5, there is a tentative detection of a reflection effect on the secondary.

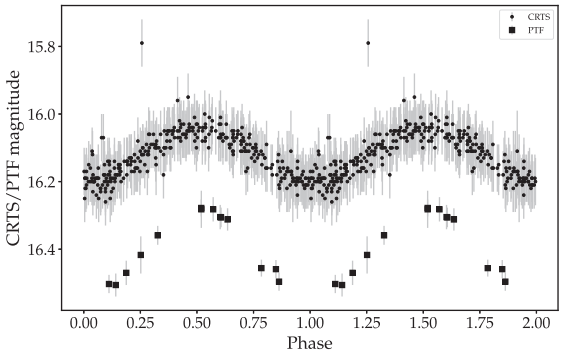

Figure 7. The phased-folded light curve of WD 1458+171 with photometry taken from the CRTS and PTF data. The modulation is attributed to a reflection effect on the secondary. PTF data points are shown with a square symbol and have not been offset from the CRTS data points. It should be noted that CRTS and PTF do not have the same passband for their photometry.

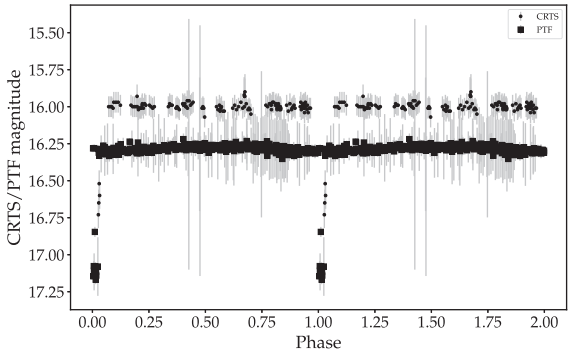

Figure 8. The phase-folded light curve of WD 1504+546 with photometry taken from the PTF and CRTS surveys.

is likely due to accretion from a stellar wind emanating from the secondary.

0430+136. This is a suspected triple, with one component resolved by *HST* and a second identified on the basis of *I*-band photometric excess at the location of the white dwarf (Farihi et al. 2010). We took 30 spectra of this target over a 1.2 yr period and can see no obvious variability above our measurement errors. However, the two components resolved by *HST* are separated by 0".26, which is several times smaller than typical seeing at Roque de Los Muchachos. Thus, it is suspected that the Na I line detected in the INT spectra originates in the brighter, widely separated, red dwarf component. If this target is followed up, then it would be more prudent to search for radial velocity variations in the Hα emission expected from the illuminated surface of the fainter red dwarf that is closer to the white dwarf.

1133+358. This is a rare DC+dM binary (Farihi et al. 2010). The fact that the pair was unresolved with ACS implies a projected separation of less than 1.3 au. Assuming canonical mass values for both of the components, an estimate for their separation is 0.06 au. The white dwarf in this system is likely to be accreting metals from the wind of the M dwarf and this therefore makes it a good target for follow-up investigations looking for metal pollution.

1333+487. This was identified as a potential triple system by Farihi et al. (2010) and has a resolved red dwarf companion at a separation of 3 arcsec with the other component being an unresolved WD+MS binary. We have successfully determined the period of this binary in this study. During our observations, we also took three spectra of the resolved red dwarf. Two spectra were taken within 15 min of each other and have radial velocities of 16 $\pm$ 1 and 20 $\pm$ 2 km s^{-1}, respectively. The third spectrum was taken 4 d later and has a radial velocity of 0 $\pm$ 1 km s^{-1}. There is a possibility that this resolved component is also a binary. Follow-up observations of this object should include spectra of the resolved red dwarf component. The *Gaia* DR2 published proper motions and parallaxes for both components agree to the extent that they are a common proper motion pair, with the small differences explicable in terms of mutual orbital motion. Their parallaxes lead to a minimum separation of $\approx$110 au.

1433+538. Although Schultz, Zuckerman & Becklin (1996) noted that the Hα region was featureless during their observations, Farihi et al. (2010) remarked that close inspection of the SDSS spectrum showed some tentative evidence of Hα and Na 8190 Å emission that may be due to noise. In this study, we did not find any evidence of emission.

1458+171. Nebot Gómez-Morán et al. (2011) identify this as a wide binary, based on two spectra taken on the same night approximately 15 min apart. Our Lomb–Scargle analysis has several competing aliases and the frequency for the minimum chi-squared value leads to a period of 0.079 d. The photometric data from the CRTS and the PTF surveys reveal a clear reflection effect on the secondary and a Lomb–Scargle analysis of these data leads to a best period of 0.164 d, which is double the period of our minimum chi-squared analysis. We have used this longer period as our result. The white dwarf has a temperature of 22 000 K and with such a short period, a reflection effect is expected. Fig. 7 shows a phase-folded plot of the CRTS and PTF data.

1504+546. The CRTS and PTF photometric data for this target are shown in Fig. 8. It is an eclipsing binary with a primary eclipse lasting 35 min. Although no secondary eclipse is visible there is a reflection effect caused by irradiation of the primary on to the inward facing hemisphere of the secondary.

Photometry of the primary eclipse for WD 1504+546 was obtained on the Liverpool telescope using the RISE camera with the RISE filter and is shown in Fig. 9. This displays a sharp ingress and egress of the white dwarf behind the secondary with a total eclipse time of 35.205 min. Approximate apparent magnitudes were calculated by comparing the flux counts with the published SDSS *r*-band magnitude of a comparison star, SDSS J150618.53+542801.5, located 114 arcsec to the east of the target. The RISE filter is a broad-

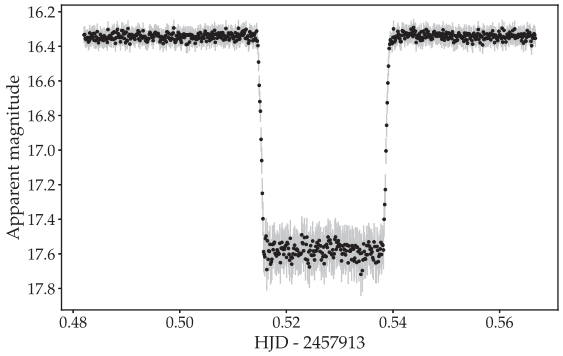

Figure 9. The Liverpool RISE camera light curve for the primary eclipse of WD 1504+546. Integration times were 2 s and the points plotted here were binned by a factor of 5.

band $V + R$ filter (covering 5000–8000 Å) and so the apparent magnitude is only approximate.

1517+502. This system was discovered by Liebert et al. (1994) and is a DA white dwarf paired with a dwarf carbon (dC) star. Farihi et al. (2010) failed to resolve the components with the *HST* ACS imaging and set a minimum separation of about 20 au. Although Liebert et al. (1994) noted a weak Na D feature at 5890 Å, and this is confirmed in the SDSS spectrum, our spectra did not show any Na I doublet at 8190 Å and we were unable to use our fitting method to determine radial velocities. The SDSS spectrum shows clear H α emission and this feature might be used in future observations.

5 CONCLUSIONS

We have measured the orbital periods and their distribution for 16 WD+MS binaries identified as likely to be PCEB binaries in Farihi et al. (2010). The periods range from 0.14 to 9.16 d and the overall distribution is similar to that encountered in previous studies of such populations (Nebot Gómez-Morán et al. 2011). Our sample does not contain any system with a period longer than 9 d. The longest period in the Nebot Gómez-Morán et al. (2011) survey is 4.3 d while the longest known period in a PCEB is that of IK Peg at 21.72 d (Landsman 1993). Three of our targets did not show significant radial velocity shifts. It is possible that these targets have periods of around 10 d and longer and therefore the radial velocity amplitudes that are too low to be detected by our particular instrument set-up.

Combining the results of Farihi et al. (2010) and this study, we can confirm the bimodal nature of the period distribution of WD+MS binaries. In their BPS study, Davis et al. 2010 predict a tail of PCEB periods longer than tens of days although more recent studies such as Toonen & Nelemans 2013 show that for certain choices of $\alpha_{\rm CE}$, in particular, choosing a low value for the efficiency of the transfer of the orbital energy into dispersing the common envelope, the BPS models predict no systems with orbital periods longer than 10 d. Although we see a sharp reduction in the number of systems with these sorts of periods, we are not able to completely rule out the possibility of a small number of systems with periods in this regime.

When comparing our results to another observational study (Nebot Gómez-Morán et al. 2011), we find no statistical difference between our distributions. Our selection was made by selecting candidates from infrared excess in the 2MASS colours and the SDSS study selected candidates by examining spectra.

ACKNOWLEDGEMENTS

The research leading to these results has received funding from the European Research Council under the European Union's Seventh Framework Programme (FP/2007–2013)/ERC Grant Agreement no. 320964 (WDTracer). Telescope time was awarded by the PATT allocation of the UK STFC. TRM was supported by the UK STFC grants ST/P000495 and ST/L000733. Data for this paper have been obtained under the International Time Programme of the CCI (International Scientific Committee of the Observatorios de Canarias of the IAC) with the Liverpool Telescope (LT) operated on the island of La Palma in the Observatorio del Roque de los Muchachos.

This work has made use of data from the European Space Agency (ESA) mission *Gaia* (https://www.cosmos.esa.int/gaia), processed by the Gaia Data Processing and Analysis Consortium (DPAC; https://www.cosmos.esa.int/web/gaia/dpac/consortium). Funding for the DPAC has been provided by national institutions, in particular the institutions participating in the Gaia Multilateral Agreement.

REFERENCES

Alam S. et al., 2015, ApJS, 219, 12
Belczynski K., Perna R., Bulik T., Kalogera V., Ivanova N., Lamb D. Q., 2006, ApJ, 648, 1110
Camacho J., Torres S., García-Berro E., Zorotovic M., Schreiber M. R., Rebassa-Mansergas A., Nebot Gómez-Morán A., Gänsicke B. T., 2014, A&A, 566, A86
Cumming A., Marcy G. W., Butler R. P., 1999, ApJ, 526, 890
Davis P. J., Kolb U., Willems B., 2010, MNRAS, 403, 179
De Marco O., 2009, PASP, 121, 316
Drake A. J. et al., 2014, ApJS, 213, 9
Dufour P., Blouin S., Coutu S., Fortin-Archambault M., Thibeault C., Bergeron P., Fontaine G., 2017, in Tremblay P.-E., Gaensicke B., Marsh T., eds, ASP Conf. Ser. Vol. 509, The Montreal White Dwarf Database: A Tool for the Community. Astron. Soc. Pac., San Francisco, p. 3
Eggleton P. P., Tokovinin A. A., 2008, MNRAS, 389, 869
Farihi J., Hoard D. W., Wachter S., 2006, ApJ, 646, 480
Farihi J., Hoard D. W., Wachter S., 2010, ApJS, 190, 275
Gaia Collaboration, 2018, A&A, 616, A1
Han Z., Podsiadlowski P., 2004, MNRAS, 350, 1301
Ivanova N. et al., 2013, A&AR, 21, 59
Landsman W., Simon T., Bergeron P., 1993, PASP, 105, 841
Law N. M. et al., 2009, PASP, 121, 1395
Liebert J., Bergeron P., Holberg J. B., 2005, ApJS, 156, 47
Liebert J., Schmidt G. D., Lesser M., Stepanian J. A., Lipovetsky V. A., Chaffe F. H., Foltz C. B., Bergeron P., 1994, ApJ, 421, 733
Lomb N. R., 1976, Ap&SS, 39, 447
Marsh T. R., 1989, PASP, 101, 1032
Marsh T. R., 1990, ApJ, 357, 621
Marsh T. R., Dhillon V. S., Duck S. R., 1995, MNRAS, 275, 828
Maxted P. F. L., Jeffries R. D., Oliveira J. M., Naylor T., Jackson R. J., 2008, MNRAS, 385, 2210
McCook G. P., Sion E. M., 1999, ApJS, 121, 1
Morales-Rueda L., Maxted P. F. L., Marsh T. R., North R. C., Heber U., 2003, MNRAS, 338, 752
Nebot Gómez-Morán A. et al., 2011, A&A, 536, A43
Nelemans G., Tout C. A., 2005, MNRAS, 356, 753
Rebassa-Mansergas A. et al., 2012, MNRAS, 423, 320
Scargle J. D., 1982, ApJ, 263, 835
Scholz F. W., Stephens M. A., 1987, J. Am. Stat. Assoc., 82, 918
Schreiber M. R., Gänsicke B. T., Southworth J., Schwope A. D., Koester D., 2008, A&A, 484, 441
Schreiber M. R. et al., 2010, A&A, 513, L7
Schultz G., Zuckerman B., Becklin E. E., 1996, ApJ, 460, 402

Tappert C., Gänsicke B. T., Zorotovic M., Toledo I., Southworth J., Papadaki C., Mennickent R. E., 2009, A&A, 504, 491
Toonen S., Nelemans G., 2013, A&A, 557, A87
Tremblay P.-E., Bergeron P., 2007, ApJ, 657, 1013
Wachter S., Hoard D. W., Hansen K. H., Wilcox R. E., Taylor H. M., Finkelstein S. L., 2003, ApJ, 586, 1356
Willems B., Kolb U., 2004, A&A, 419, 1057
Zorotovic M., Schreiber M. R., García-Berro E., Camacho J., Torres S., Rebassa-Mansergas A., Gänsicke B. T., 2014, A&A, 568, A68
Zorotovic M., Schreiber M. R., Gänsicke B. T., Nebot Gómez-Morán A., 2010, A&A, 520, A86
Zorotovic M. et al., 2011, A&A, 536, L3
Zuckerman B., Koester D., Reid I. N., Hünsch M., 2003, ApJ, 596, 477

SUPPORTING INFORMATION

Supplementary data are available at *MNRAS* online.

Please note: Oxford University Press is not responsible for the content or functionality of any supporting materials supplied by the authors. Any queries (other than missing material) should be directed to the corresponding author for the article.

APPENDIX A: ADDITIONAL TABLES

In the appendix we include a list of nightly observations and a sample of the radial velocity measurements for each object. The full radial velocity data are available online.

Table A1. Spectroscopic configurations used in this study. The instrument used was the IDS mounted on the 2.5 m Isaac Newton Telescope at the Roque de los Muchachos observatory on the island of La Palma, Spain.

Date	HJD	Grating	Central wavelength
2015/02/10	2457064	R831R	8300 Å
2015/02/11	2457065	R831R	8300 Å
2015/02/12	2457066	R831R	8300 Å
2015/02/13	2457067	R831R	8300 Å
2015/02/14	2457068	R831R	8300 Å
2015/02/15	2457069	R831R	8300 Å
2015/02/16	2457070	R831R	8300 Å
2015/02/17	2457071	R831R	8300 Å
2015/09/03	2457269	R831R	8200 Å
2015/09/04	2457270	R831R	8200 and 6562 Å
2015/09/05	2457271	R831R	8200 and 6562 Å
2015/09/06	2457272	R831R	8200 and 6562 Å
2015/09/07	2457273	R831R	8200 and 6562 Å
2015/09/08	2457274	R831R	8200 and 6562 Å
2016/02/12	2457431	R831R	8022 and 6565 Å
2016/02/13	2457432	R831R	8022 and 6565 Å
2016/02/14	2457433	R831R	8022 and 6565 Å
2016/02/29	2457448	R831R	8022 and 6565 Å
2016/03/01	2457449	R831R	8022 and 6565 Å
2016/03/02	2457450	R831R	8022 and 6565 Å
2018/06/18	2458298	R831R	8190 Å

Table A2. Standards used for flux calibration and telluric removal.

Date	Standards observed
2015/02/10	Feige 34, BD+26 2606
2015/02/11	Feige 34, BD+26 2606
2015/02/12	HD 19445, HR1342
2015/02/13	BD+26 260, HR6110, HR1342
2015/02/14	HR6110, HD 93521, HZ 15
2015/02/15	HD 84937, HR3958, HD 93521
2015/02/16	HR6110, HD 93521
2015/02/17	HD 19445, HR6110, HD 93521
2015/09/03	Wolf 1346, G191-B2B
2015/09/04	Wolf 1346, G191-B2B
2015/09/05	Wolf 1346, G191-B2B
2015/09/06	Wolf 1346, G191-B2B
2015/09/07	Wolf 1346, G191-B2B
2015/09/08	Wolf 1346, G191-B2B
2016/02/12	G191-B2B, Grw+70 5824
2016/02/13	G191-B2B, Grw+70 5824
2016/02/14	G191-B2B, Grw+70 5824
2016/02/29	G191-B2B, Grw+70 5824
2016/03/01	G191-B2B
2016/03/02	G191-B2B, Grw+70 5824
2018/06/18	Feige 98, Grw+70 5824, L1512-34

APPENDIX B: RADIAL VELOCITY FIGURES

Table B1. The measured radial velocities of our targets from a fit of a double-Gaussian to the Na I doublet at 8190 Å. This table is abridged. The full data are available at Vizier.

WD	HJD	Radial velocity ($km\,s^{-1}$)	Error ($km\,s^{-1}$)
0023+388	2457066.347907	− 28.5	0.8
0023+388	2457066.358477	− 27.2	0.9
0023+388	2457269.503428	87.3	5.1
0023+388	2457269.510507	85.0	6.2
0023+388	2457270.542192	− 166.8	3.9
0023+388	2457270.549273	− 168.9	3.5
0023+388	2457271.597316	76.7	3.9
0023+388	2457271.604397	71.1	4.0
0023+388	2457272.511428	− 154.5	3.9
0023+388	2457272.518510	− 171.0	4.9
0023+388	2457273.500880	82.6	4.8
0023+388	2457273.507961	99.8	4.8
0023+388	2457274.493951	− 115.5	8.4
0023+388	2457274.501032	− 114.2	5.7
0023+388	2457432.344926	− 69.2	10.4
0023+388	2457432.352005	− 80.5	11.1
0023+388	2458298.655991	120.5	7.6
0023+388	2458298.663180	140.3	6.6
0023+388	2458298.677734	128.8	7.4
0303−007	2457066.373914	137.3	3.4
0303−007	2457066.384616	136.0	2.8
0303−007	2457067.339107	39.7	2.0
0303−007	2457067.349969	52.1	2.1
0303−007	2457068.350021	− 73.0	2.2
0303−007	2457070.350993	− 47.9	3.5
0303−007	2457070.361546	− 65.9	3.2
0303−007	2457071.350476	50.6	3.5
0303−007	2457071.361029	26.1	4.7
0303−007	2457269.608182	− 113.8	5.0
0303−007	2457269.615262	− 121.9	4.5
0303−007	2457270.602259	− 105.6	2.6
0303−007	2457270.609340	− 112.5	2.5
0303−007	2457271.634996	− 61.6	2.8
0303−007	2457271.642077	− 73.7	3.0
0303−007	2457272.580913	124.4	2.4
0303−007	2457272.587994	123.9	2.2
0303−007	2457272.710581	− 13.5	2.4
0303−007	2457272.717661	− 23.9	2.1
0303−007	2457273.586402	118.5	2.9
0303−007	2457273.593485	133.0	2.7

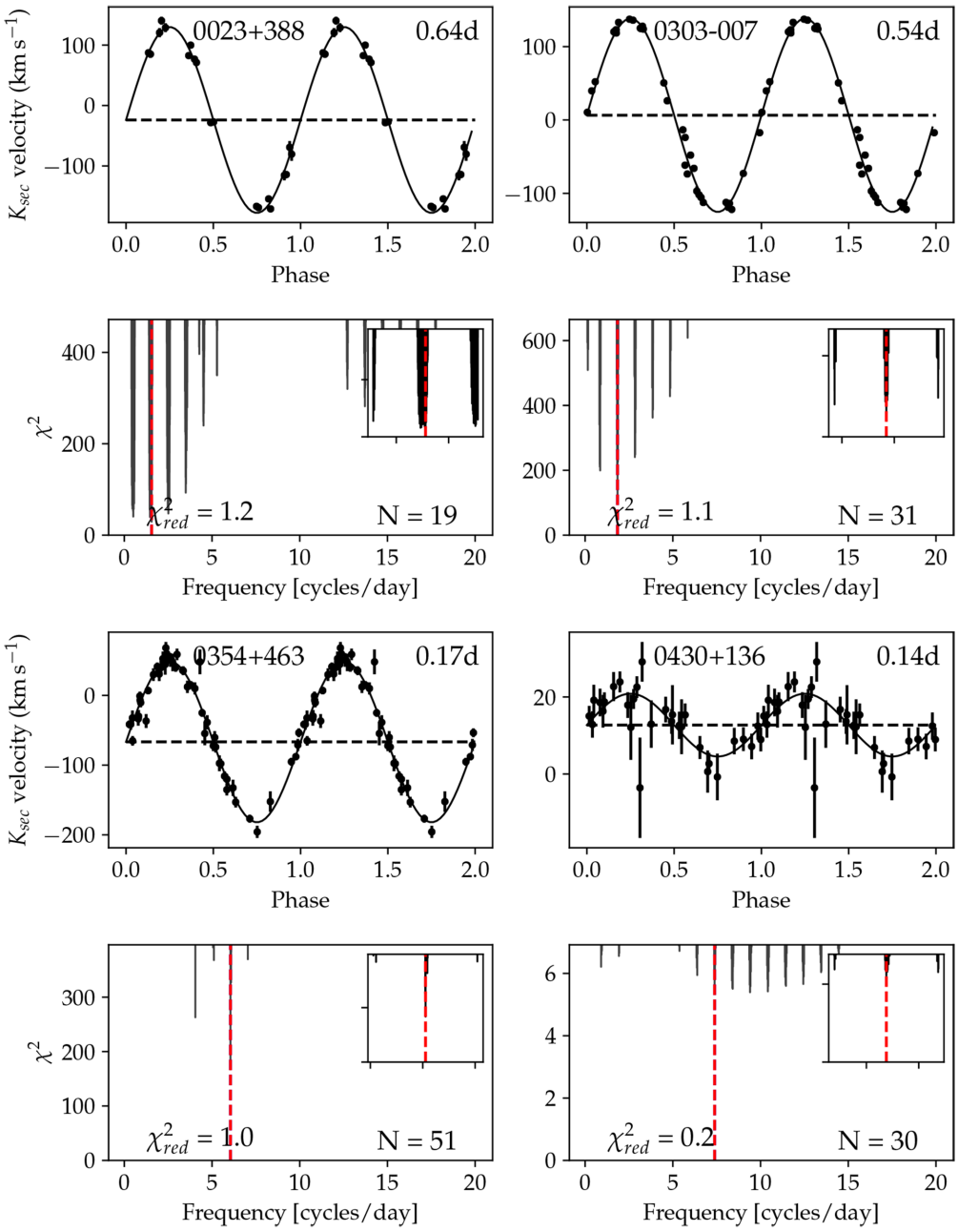

Figure B1. Plot of the 19 radial velocity fits. For each object depicted, the upper plot shows the radial velocity in km s^{-1} as a function of phase and the lower plot shows the χ^2 (after fitting a sinusoid plus a constant to the data) as a function of frequency. The vertical red line on the periodograms is the frequency chosen as the best fit and the period used for the folded radial velocity curve is derived from this. The insets to the periodograms show a zoomed in region near the best-fitting period, spanning a region of ±10 per cent around the chosen frequency. A blue vertical line is shown where we found a second competing alias has a good chance of being the true period. See notes on individual objects for a discussion.

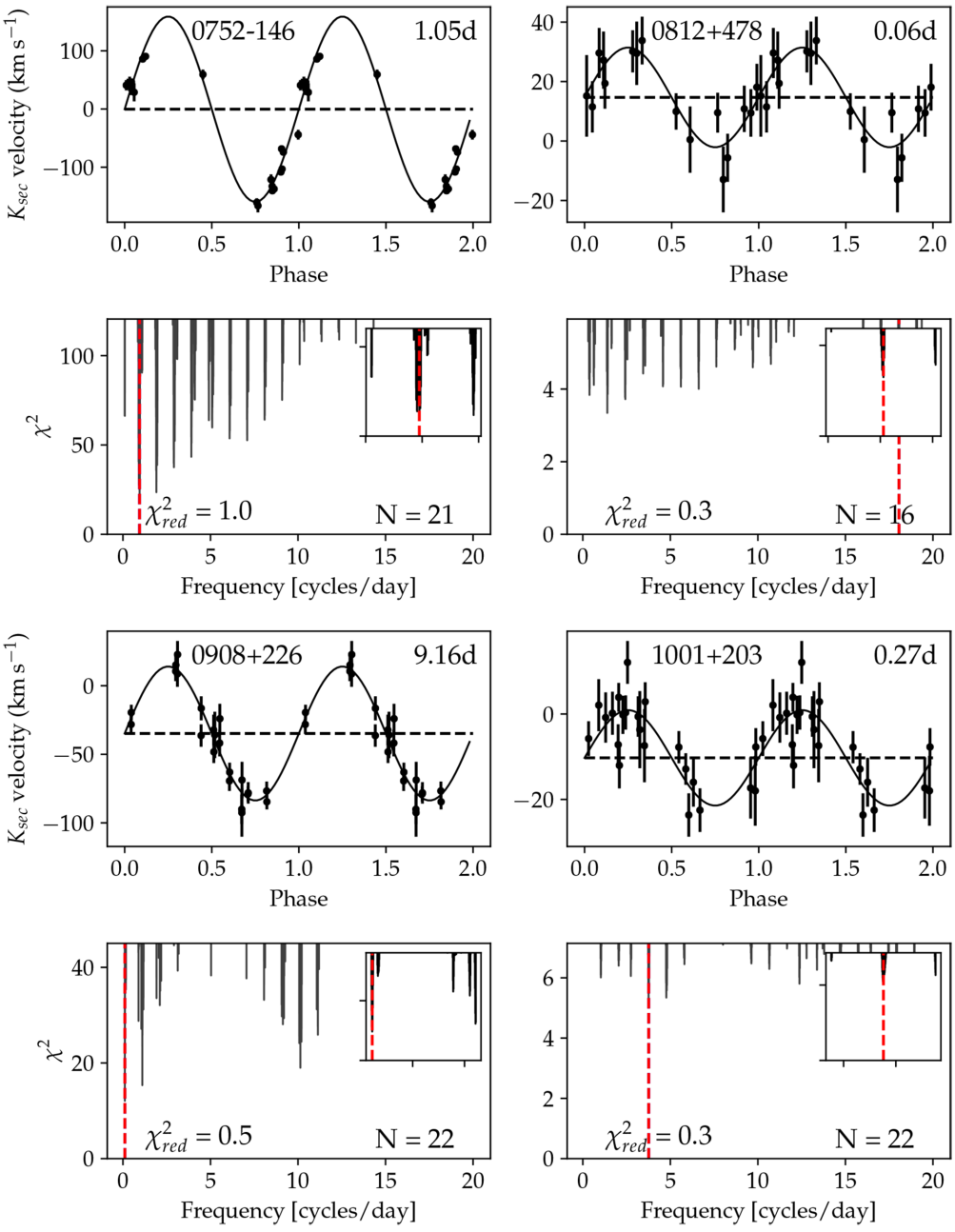

Figure B1 – *continued*

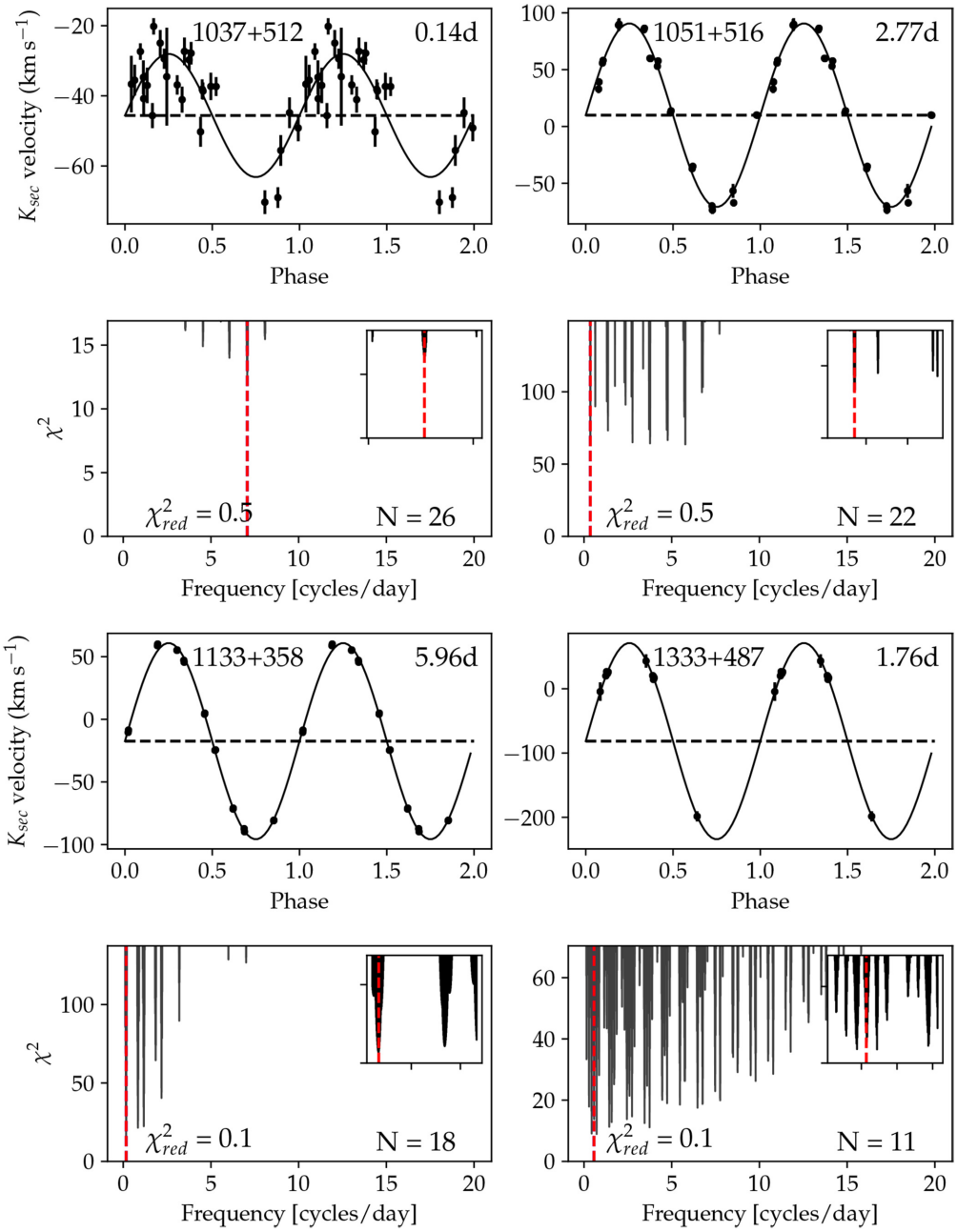

Figure B1 – *continued*

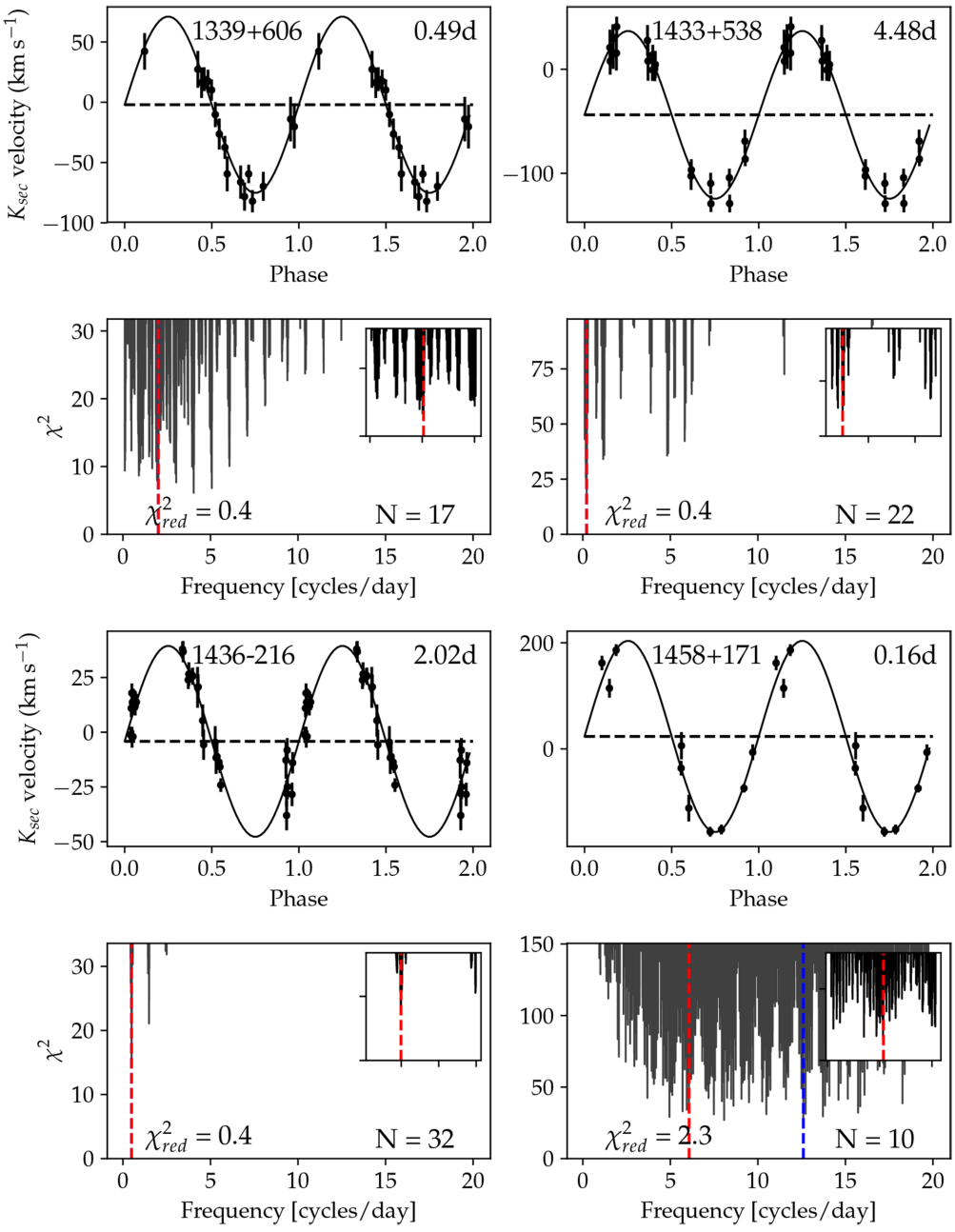

Figure B1 – *continued*

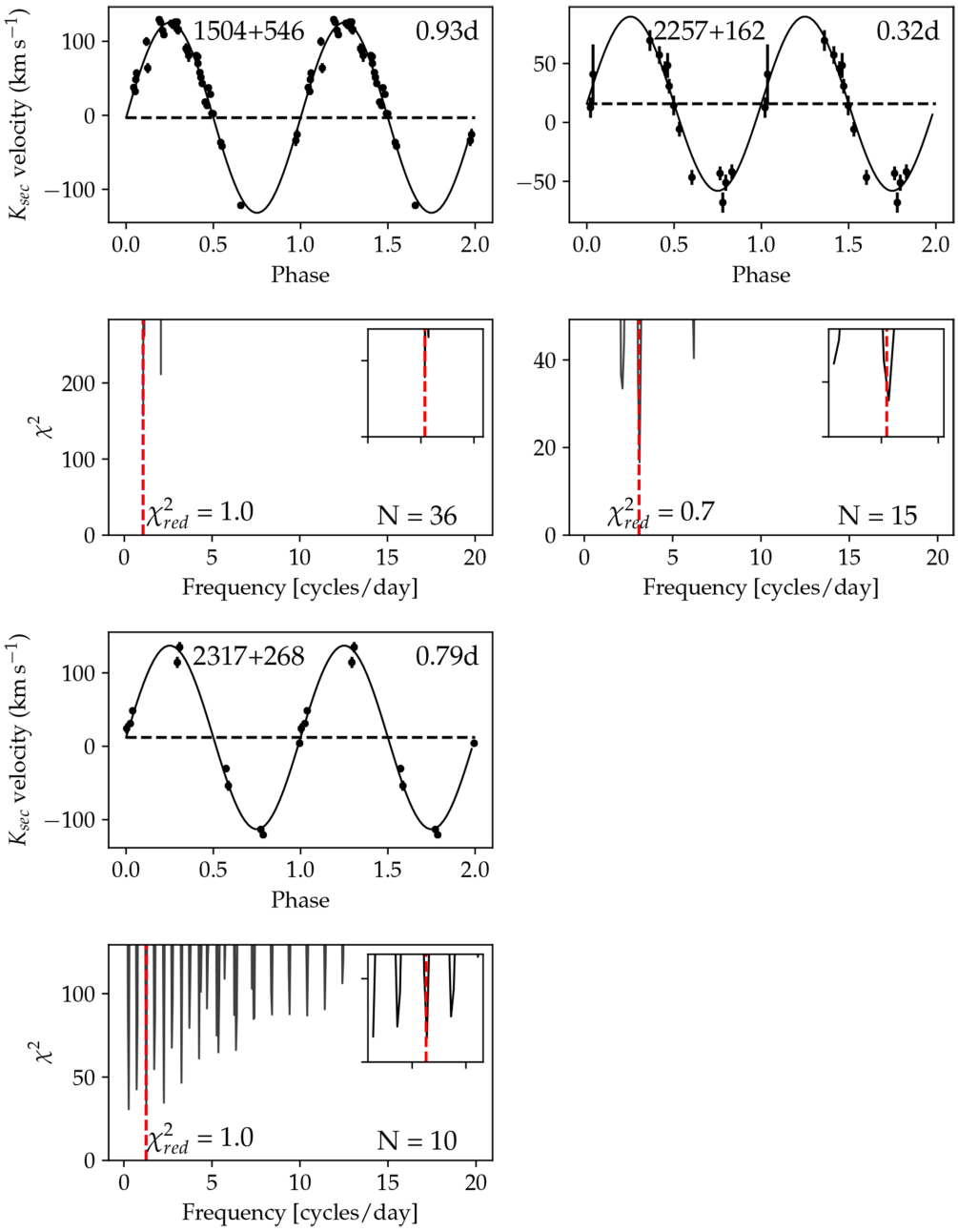

Figure B1 – *continued*

This paper has been typeset from a TEX/LATEX file prepared by the author.